Zhu, X., et al., 2023, Massive rare earth element storage in sub-continental lithospheric mantle initiated by diapirism, not by melting: Geology, https://doi.org/10.1130/G51102.1

Supplemental Material

Supplemental text.

Tables S1–S5.

Figures S1–S5.

Starting materials

Marine sediments often exhibit complex mineral assemblages, chemical compositions and REE host, among which REE-rich marine sediments contain substantial pelagic REE resources (e.g., Liao et al., 2022; Ren et al., 2021; Ren et al., 2022) and was considered as the main contributors to REE-bearing rocks (Hou et al., 2015). Although the main hosts of marine REEs are proposed to be Ca-phosphate and Fe-Mn oxides etc., they account for a only low proportion of marine sediments, which are difficult to contribute large amount of REEs for the formation of REE-bearing rocks. Thus, clay-rich marine sediments, as the majority of REE-rich marine sediments, were selected as starting materials of our experiments.

We used three representative natural REE-rich marine sediments from Pigafetta Basin, western Pacific. The chemical compositions as well as the mineral assembles of them are listed in Table S1 and Table S2. These three sediments are mainly consist of clay minerals, including Fe-chlorite, montmorillonite, illite and pyrophyllite (Table S2) while in different proportions. We specifically choose samples with different mineral compositions to test how robust our results are with respect to compositions. For example, sample 64-30 are mainly composed of andesine (39.35%), montmorillonite (28.41%) and illite (20.01%); sample 64-46 contains anorthite (30.10%), andesine (25.15%) and illite (16.99%); and sample 64-55 contains anorthite (30.30%), illite (28.40%) with 19.5% of andesine (Table S2). Apatite in these samples vary from 1.17–4.45% (Table S2). Such various mineral assemblages

can cover mostly REE-rich marine sediments worldwide (Liao et al., 2022; Ren et al., 2021; Ren et al., 2022).

Additionally, based on the comparisons of among >8000 global samples (Ren et al., 2021), the REE+Y contents of marine sediments are of 8–7974 ppm, but the main distribution is between ca. 140–3000 ppm. The selected samples could properly cover these REE variations, with REE+Y contents of 960 to 2039 ppm (Table S1). All three samples show high Al_2O_3, Na_2O, K_2O, F and Cl contents and contains ca. 10% H_2O (Table S1). The C_{total} of the three sediments was 0.14–0.16 wt.%. The first sample (64-30) is a pristine pelagic sediment and contains the highest ∑REE value (1421 ppm; Table S1) and clay minerals proportion (54.48 wt.%; Table S2). The second sample (64-46) shows the highest A/CNK [Al_2O_3/(CaO+Na_2O+K_2O)] value (1.05) and SiO_2 content, while low in ∑REE (715 ppm; Table S2). The third sample (64-55) is characterized by elevated F and $Fe_2O_3^T$, as well as relatively low Al_2O_3 and K_2O contents. This sample contains greater apatite proportions (4.45 wt.%; Table S2).

High-temperature experiments

Generally, REE resources are mostly hosted by alkaline-silicate rocks and carbonatites derived from REE-rich mantle sources fertilized by subduction while formed in intracontinental, rift-related and syn- to post-collisional settings (Goodenough et al., 2021; Beard et al., 2023). Hou et al (2015) realized such two-stage REE migration process, and explained the delayed melting of these REE-rich sources, as hindered by SCLM thick enough (>2.5 GPa). However, such model dispalys inherent irrationalities, as it is unlikely that each REE-rich sources could

coincidentally encounter a SCLM thick enough, hindering its erupting. Thus, combining with the suggested pressure ranges of 2–4 GPa, approximately to the depth of 60–120 km, where diapirism forms presumably (Behn et al., 2011), we setted our experiments at among 3–4 GPa. The starting temperature starting are setted at 800°C, mainly refers to the experimentally determined temperature where most sediments remain in solid (Schmidt, 2015) and recent thermal models of slab-top conditions beneath arcs (Cooper et al., 2012; Syracuse et al., 2010; van Keken et al., 2002). We then gradually increase the temperature in a gradient of 100°C in the same pressure until the melting behaviors or indications occur. We carried out experiments at 3–4 GPa and 800–1000°C, aiming to constrain the changes in phase relations of these sediments and the REE migrating behaviors, under subduction zones.

The starting materials were repeatedly ground with a mortar and pestle and then dried at 120°C for 48 h before loading into capsules. Experiments were carried out using a CS-IV 6×14 MN cubic press at the High Pressure and High Temperature laboratory, Peking University. The experimental assembly (BJC-11) employs a pyrophyllite cube with an edge length of 32.5 mm and an inner cylindrical unit comprising of a boron nitride (BN) outer sleeve, graphite heater, and a BN/MgO spacer and capsule sleeve. The starting materials were loaded into small capacity (2.0 mm diameter and 2.0 mm height) $Au_{80}Pd_{20}$ capsules for experiments. Temperature was monitored using a type-C (WRe_5-WRe_{26}) thermocouple. Both pressure and temperature were controlled automatically. Pressure was initially raised to the target value followed by temperature increase at a rate of 100°C/min. The experiments were

quenched by cutting off power while pressure was maintained for a further 20 minutes before a slow decompression to ambient pressure. The run durations were 24–120 h (Table S3). Recovered capsules were cut into halves along the axial direction. Half of the capsule was then mounted in epoxy resin, polished with kerosene and carbon coated for further analysis.

Analytical methods

The major element compositions of the sediments were determined by X-ray fluorescence (XRF). Inductively coupled plasma-mass spectrometry (ICP-MS) was used to analyze the trace elements and REE. Micro-focused X-ray diffractometer (XRD, M18XHF) was used to assist identifying the mineral proportion of the sediments. The bulk H_2O content of starting materials were based on the loss on ignition values (Table S1).

Polished run products were imaged using a JEOL JSR-1000 scanning electron microscope (SEM). Major elements of garnet, apatite, clinopyroxene, quartz, mica, K-feldspar and silicate melt were measured using JXA-8100 electron probe microanalyzer (EPMA). Operating conditions were 15 kV accelerating voltage and a current of 12 nA with peak counting times between 20 and 30 s for analyses of silicate melt. Garnet, apatite, clinopyroxene, quartz, K-feldspar and mica were measured at 20 kV and 30 nA with peak counting times of 150 s to access minor element concentrations. The beam diameter for garnet, apatite, clinopyroxene, quartz, K-feldspar and mica was 2 μm. Due to the chemical heterogeneity caused by quenching

of silicate melt, we used a larger beam diameter of 10 μm for analyzing major elements of silicate melt.

Trace elements and REE of garnet, apatite, clinopyroxene, mica, K-feldspar and silicate melt were measured by laser ablation inductively coupled plasma mass spectrometry (LA-ICP-MS), using a GeolasPro laser ablation system (wavelength 193 nm, maximum energy 200 mJ). An Agilent 7700e ICP-MS instrument was used to acquire ion-signal intensities. The spot size and frequency of the laser were set to 30 μm and 5 Hz, respectively. Each analysis incorporated a background acquisition of approximately 20–30 s followed by 50 s of data acquisition from the sample. Trace element compositions of minerals were calibrated against various reference materials (BHVO-2G, BCR-2G and BIR-1G). Off-line selection and integration of the background and the analyzed signals, as well as time-drift correction, and quantitative calibration were performed by ICPMSDataCal (Liu et al., 2008).

Mass balance calculation

Based on mass balance calculations, we obtained the modal abundances and proportions of each phase (Table S3). The phase proportions (M) were obtained by solving the following equations to minimize the $\sum R^2$:

$$C^i_{bulkC} = \sum_n^{phase}\left[M_n \times C^i_n\right] \quad (1)$$

$$\sum R^2 = \sum_i^{component}\left[C^i_{bulkC} - C^i_{bulkS}\right]^2 \quad (2)$$

Where i = SiO_2, Al_2O_3, MgO, CaO, Na_2O, K_2O, MnO, TiO_2 and P_2O_5; n = silicate melt, garnet, apatite, clinopyroxene, mica, K-feldspar and quartz/coesite; C^i_{bulkC} = the calculated bulk concentration of component i in the system; C^i_n = the

measured component i concentration of phase n; C^{i}_{bulkS} = the i concentration of the starting material in the capsule. To reduce the effect of heterogeneous compositions, we obtained the average chemical composition of many analyses, the detailed results are presented in Table S3.

Phase compositions

Major and trace element compositions of all the run products are given in Table S4, Table S5 and Figure S2 to Figure S5. Garnets in all run products are compositionally similar, being rich in almandine (19.16–72.38%), pyrope (6.24–42.04%), spessartine (11.99–40.85%) and grossular (1.24–13.88%), but poor in andradite (0.00–12.44%, Table S4, Figure S2). Generally, all the garnets exhibit negative anomalies for Ce, Nb, Sr, Zr and Hf, and depleted in light REE (LREE) at all temperatures. HREE abundance in garnet is lower at 3 GPa, 900℃ experiments. The cerium anomalies are inherited from the similarly Ce-anomalous starting material, and do not indicate exceptional oxidising conditions during the experimental runs.

Clinopyroxenes are primarily jadeitic (42.07–89.06% in sample 64-30, 44.45–88.68% in sample 64-46 and 33.47–84.04% in sample 64-55), whereas the quadrilateral component (Ca-Mg-Fe) component is much lower (10.94–57.93% in sample 64-30, 11.32–50.98% in sample 64-46 and 15.26–66.53% in sample 64-55). A small but significant calculated aegirine component occurs only in sample 64-55 at 4 GPa, 1000℃ (5.49–23.37%; Table S4; Figure S3). REE pattern of all clinopyroxenes are relatively flat and contain inherited negative Ce anomalies (Figure S3B). The trace element patterns show negative anomalies for Sr, Nb, Ti, and U, Nd, Ta enrichment.

REE concentrations of clinopyroxene display a strong temperature dependence, being lower at higher temperatures.

Apatite occurs as a minor phase in all the experimental runs (Table S4, Figure S4), of which the calculated P content lies at 4.65–6.06 apfu, and the F and Cl content 1.07–3.96 apfu. Excess fluorine could be an analytical artifact (Stock et al., 2015). Apatite is the principal REE host, with ∑REE values as high as 22000 ppm (Table S5). Other elements also show consistent variation trend with other minerals, such as the negative anomalies for Rb, Nb, Ta, Sr, Zr, Hf and Ti, and positive anomalies for Th, and U (Figure S4).

Mica of 4 GPa experiments have relatively high content of Si > 3.5 apfu (3.52–3.77 apfu), Al content approximately to 2 apfu (1.53–1.96 apfu) and Mg + Fe values of 0.47–0.80 apfu, which could be classified as phengite (Table S4). In contrast, in the 3 GPa 900℃ experiments, exhibits lower Si (3.17–3.39 apfu), Al (0.93–1.24 apfu) content, and relatively higher Mg + Fe (1.65–2.46 apfu) and F + Cl (0.75–1.03 apfu) contents. Mica, is the only observed hydrous mineral. Its proportions decrease with increasing temperature, and disappeared as soon as the melting behaviors exist (Figure 1). It is noteworthy that, its edge is obviously dissolved, at 3 GPa 900℃ experiments, which betokens the imminent melting behaviors. In general, mica in the experimental products is relatively pure, of which the trace element contents are lower, compared to other phase (∑REE values of sample 64-30 from 214 to 6.68 ppm, sample 64-46 from 537 to 22.7 ppm and sample 64-55 from 205 to 34.5 ppm; Table S5).

K-feldspar is pure with Si of 2.98–3.02 apfu, K of 0.96–1.02 apfu, and low in Mg, Fe, F and Cl contents (Table S4). It only occurs in the 3 GPa 900℃ experiments, in form of crystal filler (Figure S1). Such experimental results are consistent with the experiments of Hermann and Spandler (2008), of which the K-feldspar exists only under low pressure runs (2.5 Gpa). ∑REE values of all the K-feldspar crystals are uniform, from 118 to 256 ppm (Table S5).

Silica phases occur in the experimental runs, but we did not differentiate quartz from coesite. Quartz/coesite is unstable at higher temperature, as it is only observed in the LMD 752-46 (sample 64-46), of all the 1000℃ runs. It is poor in trace element contents (Table S4).

We sampled all melt compositions, only observed at 1000℃. Melts are alkaline-silicate, which exhibit high concentrations of SiO_2 (50.14–58.76 wt. %), Al_2O_3 (11.25–12.26 wt.%) and Na_2O+K_2O (2.47–10.14 wt.%; Table S4). Partial melts from runs 64-30 and 64-46 are metaluminous, according to the A/CNK [Al/(Ca+Na+K)] values approximately to 1. The 64-55 partial melt is peraluminous, with higher A/CNK value of 2.62. The variable σ $[(Na_2O+K_2O)^2/(SiO_2-43)]$ values in the melts are 14.44 (64-30), 3.95 (64-46) and 0.83 wt.% (64-55) respectively. In the Figure S5A, melts of sample 64-30 and 64-46 are plotted in the trachyte field, while that of 64-55 is dacitic (Figure S5). The three melts contain different REE contents, with ~190 ppm in sample 64-30, ~500 ppm in sample 64-46, and ~60 ppm in sample 64-55 (Table S5). LREEs are enriched in the 64-30 partial melt relative to HREE. REE patterns of 64-46 and 64-55 are relatively flat except for the negative Ce

anomalies (Figure S5B). Fluid-mobile elements, such as Cs, Rb, Ba, Sr and Li are always enriched in the melts. Other incompatible elements such as U, Zr, Hf and Y are also moderately enriched (Figure S5C).

Note that LA-ICP-MS B contents in some spots (especially melts of 64-30 and 64-55) are spuriously high leaded by unknown analytical reasons, but impact minor on both sedimentary melting and the REE migrating behaviors as no B-bearing phases were observed in the produced phases, and no flux-melting behaviour was observed.

Details of the density calculation

We calculated the densities of the REE-rich marine sediments used for the starting material in our high-pressure experiments as a function of temperature and pressure using Perple_X 6.9.1 (Connolly, 2005) and compared them to the harzburgite density described by Jull and Kelemen (2001).

Figure captions for Data Repository

Figure S1. Backscattered electron (BSE) images of experimental run products. Mineral abbreviations as in Figure 1.

Figure S2. (A, B) Proportions (mol%) of different garnet end members as a function of temperature at 3–4 GPa; (C) Chondrite-normalized REE and (D) primitive-mantle-normalized trace element patterns of garnet. Normalizing values are after McDonough and Sun (1995).

Figure S3. (A) The component (mol%) in clinopyroxene as a function of temperature at 3–4 GPa; (C) Chondrite-normalized REE and (D) primitive-mantle-normalized trace element patterns of clinopyroxene. Normalizing values are after McDonough

and Sun (1995).

Figure S4. (A) Chondrite-normalized REE and (B) primitive-mantle-normalized trace element patterns of apatite. Normalizing values are after McDonough and Sun (1995).

Figure S5. (A)TAS-diagram, (B) Chondrite-normalized REE and (C) primitive-mantle-normalized trace element patterns of melts. Normalizing values are after McDonough and Sun (1995).

References for Data Repository

Behn, M. D., Kelemen, P. B., Hirth, G., Hacker, B. R., and Massonne, H. J., 2011, Diapirs as the source of the sediment signature in arc lavas: Nature Geoscience, v. 4, no. 9, p. 641–646.

Connolly, J., 2005, Computation of phase equilibria by linear programming: A tool for geodynamic modeling and its application to subduction zone decarbonation: Earth Planetary Science Letters, v. 236, no. 1–2, p. 524–541.

Cooper, L. B., Ruscitto, D. M., Plank, T., Wallace, P. J., Syracuse, E. M., and Manning, C. E., 2012, Global variations in H2O/Ce: 1. Slab surface temperatures beneath volcanic arcs: Geochemistry, Geophysics, Geosystems, v. 13, no. 3.

Goodenough, K. M., Deady, E. A., Beard, C. D., Brrom-Fendly, S., Elliott, H. A. L., Berg, F., and Qzturk, H., 2021, Carbonatites and Alkaline Igneous Rocks in Post-Collisional Settings: Storehouses of Rare Earth Elements. Journal of Earth Science, v. 32, p. 1332–1358.

Hermann, J., and Spandler, C. J., 2008, Sediment Melts at Sub-arc Depths: an

Experimental Study: Journal of Petrology, v. 49, no. 4, p. 717–740.

Jull, M., and Kelemen, P., 2001, On the conditions for lower crustal convective instability: Journal of Geophysical Research. Biogeosciences, v. 106, no. B4, p. 6423–6446.

Liao, J., Chen, J., Sun, X., Wu, Z., Deng, Y., Shi, X., Wang, Y., Chen, Y., and Koschinsky, A., 2022, Quantifying the controlling mineral phases of rare-earth elements in deep-sea pelagic sediments: Chemical Geology, v. 595, p. 120792.

Liu, Y., Hu, Z., Gao, S., Günther, D., and Xu, J., 2008, In situ analysis of major and trace elements of anhydrous minerals by LA-ICP-MS without applying an internal standard: Chemical Geology, v. 257, no. 1, p. 34–43.

McDonough, W. F., and Sun, S. S., 1995, The composition of the Earth: Chemical Geology, v. 120, no. 3, p. 223–253.

Ren, J., Jiang, X., He, G., Wang, F., Yang, T., Luo, S., Deng, Y., Zhou, J., Deng, X., Yao, H., and Yu, H., 2022, Enrichment and sources of REY in phosphate fractions: Constraints from the leaching of REY-rich deep-sea sediments: Geochimica et Cosmochimica Acta, v. 335, p. 155–168.

Ren, J., Liu, Y., Wang, F., He, G., and Yao, H., 2021, Mechanism and Influencing Factors of REY Enrichment in Deep-Sea Sediments: Minerals, v. 11, no. 196.

Schmidt, M. W., 2015, Melting of pelitic sediments at subarc depths: 2. Melt chemistry, viscosities and a parameterization of melt composition: Chemical Geology, v. 404, p. 168–182.

Stock, M. J., Humphreys, M. C. S., Smith, V. C., Johnson, R. D., and Pyle, D. M.,

2015, New constraints on electron-beam induced halogen migration in apatite: American Mineralogist, v. 100, no. 1, p. 281–293.

Syracuse, E. M., van Keken, P., and Abers, G. A., 2010, The global range of subduction zone thermal models: Physics of the Earth Planetary Interiors, v. 183, no. 1–2, p. 7390.

van Keken, P. E., Kiefer, B., and Peacock, S. M., 2002, High-resolution models of subduction zones: Implications for mineral dehydration reactions and the transport of water into the deep mantle: Geochemistry, Geophysics, Geosystems, v. 3, no. 10, p. 1056.

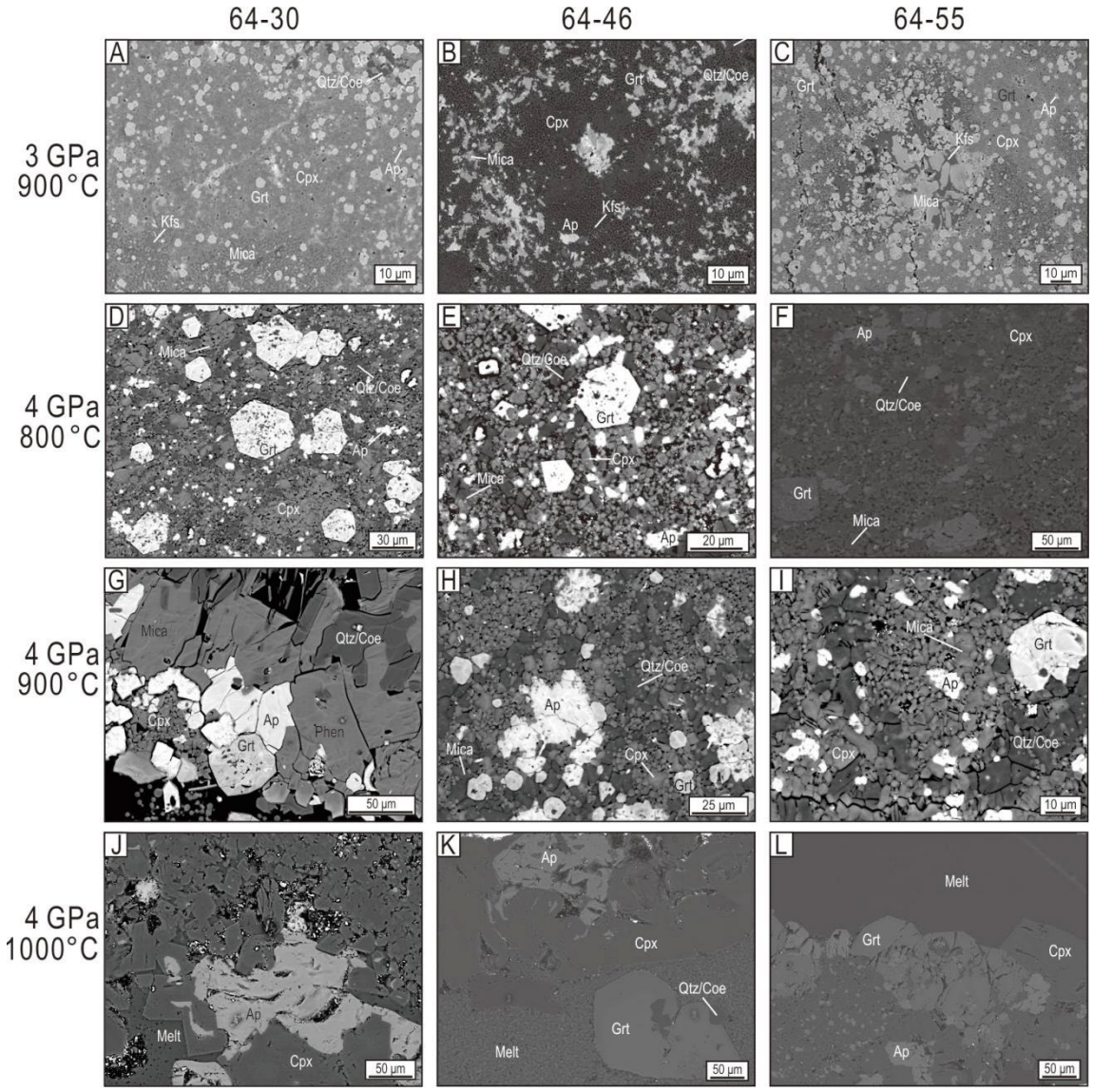
64-30
64-46
64-55
3 GPa
900 °C
4 GPa
800 °C
4 GPa
900 °C
4 GPa
1000 °C
A
B
C
D
E
F
G
H
I
J
K
L
Qtz/Coe
Cpx
Grt
Ap
Kfs
Mica
Phen
Melt
10 µm
20 µm
25 µm
30 µm
50 µm

Figure S1

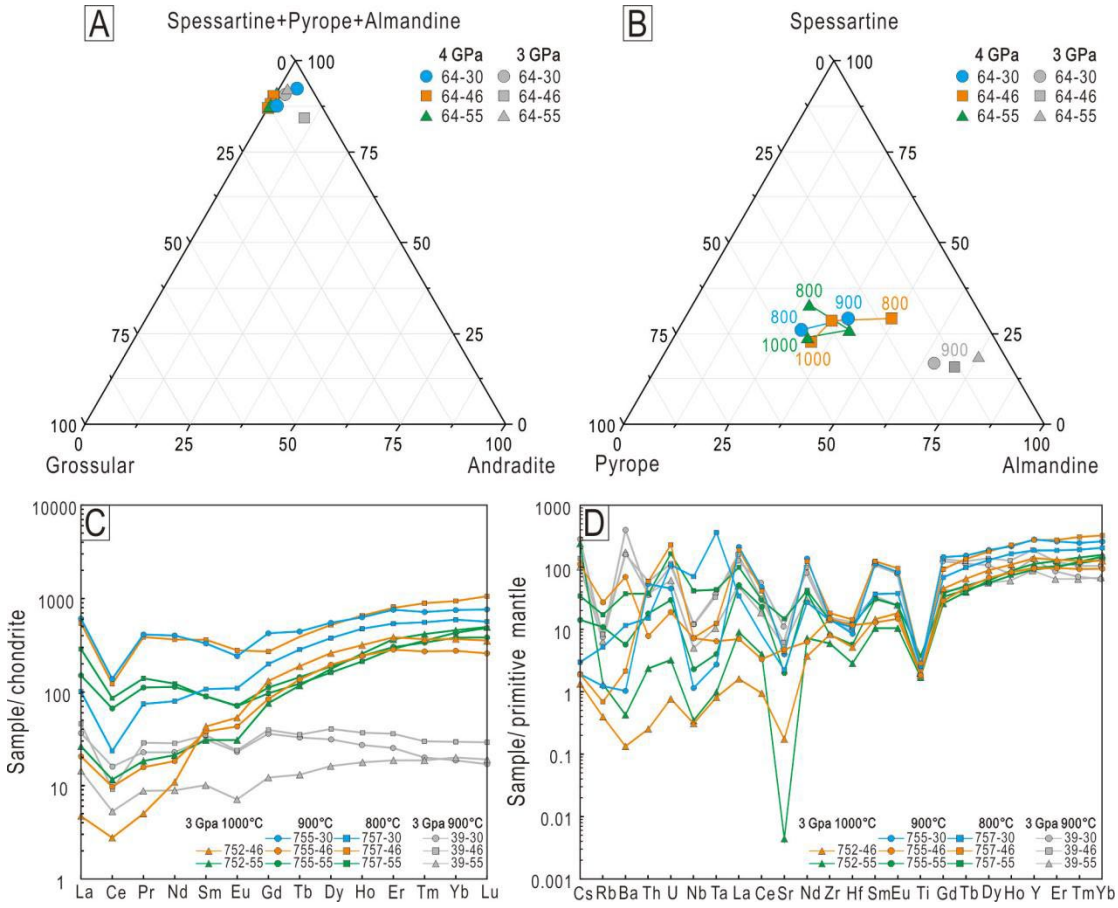
A
Spessartine+Pyrope+Almandine
4 GPa
3 GPa
64-30
64-46
64-55
Grossular
Andradite
B
Spessartine
Pyrope
Almandine
800
900
1000
C
Sample/ chondrite
3 Gpa 1000°C
900°C
800°C
3 Gpa 900°C
755-30
757-30
39-30
752-46
755-46
757-46
39-46
752-55
755-55
757-55
39-55
La Ce Pr Nd Sm Eu Gd Tb Dy Ho Er Tm Yb Lu
D
Sample/ primitive mantle
Cs Rb Ba Th U Nb Ta La Ce Sr Nd Zr Hf Sm Eu Ti Gd Tb Dy Ho Y Er Tm Yb

Figure S2

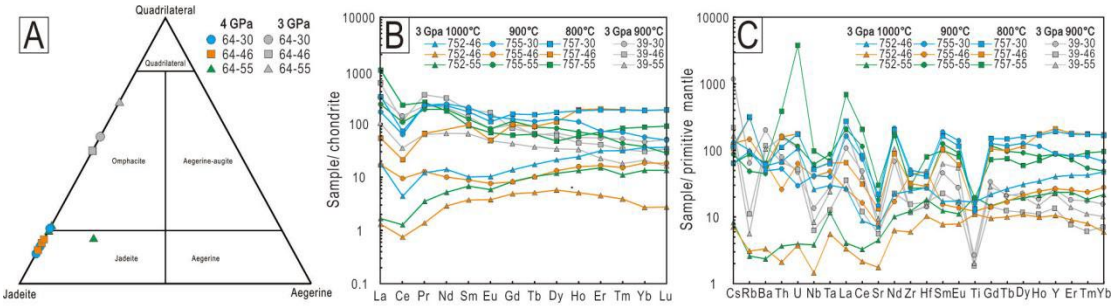
A
Quadrilateral
4 GPa
3 GPa
64-30
64-46
64-55
64-30
64-46
64-55
Omphacite
Aegerine-augite
Jadeite
Aegerine
B
3 Gpa 1000°C
900°C
800°C
3 Gpa 900°C
752-46
752-46
752-55
755-30
755-46
755-55
757-30
757-46
757-55
39-30
39-46
39-55
Sample/ chondrite
La Ce Pr Nd Sm Eu Gd Tb Dy Ho Er Tm Yb Lu
C
Sample/ primitive mantle
Cs Rb Ba Th U Nb Ta La Ce Sr Nd Zr Hf Sm Eu Ti Gd Tb Dy Ho Y Er Tm Yb

Figure S3

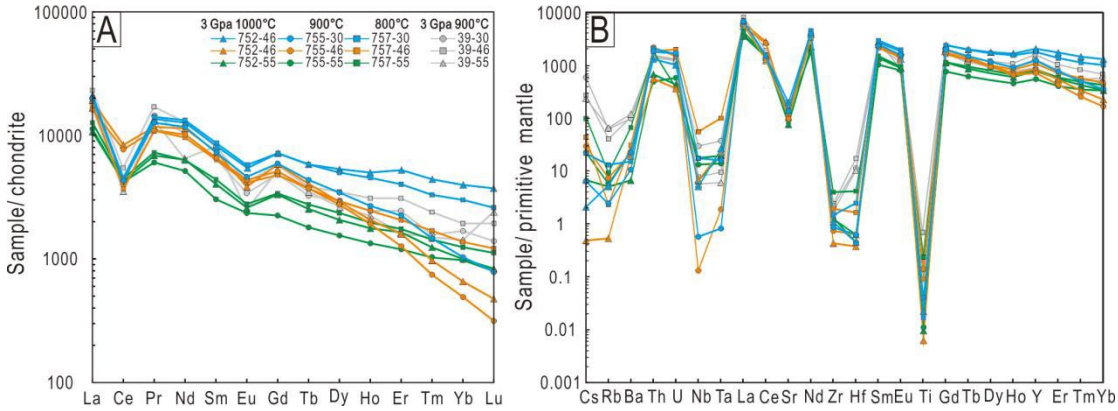
A
3 Gpa 1000°C
900°C
800°C
3 Gpa 900°C
752-46
752-46
752-55
755-30
755-46
755-55
757-30
757-46
757-55
39-30
39-46
39-55
Sample/ chondrite
100000
10000
1000
100
La Ce Pr Nd Sm Eu Gd Tb Dy Ho Er Tm Yb Lu
B
Sample/ primitive mantle
10000
1000
100
10
1
0.1
0.01
0.001
Cs Rb Ba Th U Nb Ta La Ce Sr Nd Zr Hf Sm Eu Ti Gd Tb Dy Ho Y Er Tm Yb

Figure S4

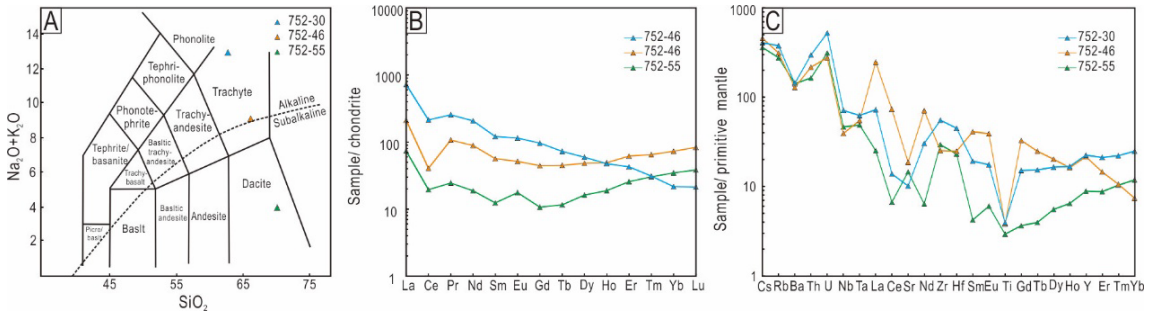
A
752-30
752-46
752-55
Phonolite
Tephri-phonolite
Trachyte
Phonote-phrite
Trachy-andesite
Alkaline
Subalkaline
Tephrite/ basanite
Basitic trachy-andesite
Trachy-basalt
Dacite
Basitic andesite
Andesite
Basalt
Picro-basalt
Na2O+K2O
SiO2
B
752-46
752-46
752-55
Sample/ chondrite
La Ce Pr Nd Sm Eu Gd Tb Dy Ho Er Tm Yb Lu
C
752-30
752-46
752-55
Sample/ primitive mantle
Cs Rb Ba Th U Nb Ta La Ce Sr Nd Zr Hf Sm Eu Ti Gd Tb Dy Ho Y Er Tm Yb

Figure S5

Table S1. Major and trace element of REE-rich marine sediment samples

Sample No.	64-30	64-46	64-55
Depth（m）	4800~6200		
Horizon（cm）	435~450	675~690	810~833
wt.%			
SiO_2	45.75	47.55	46.09
Al_2O_3	14.17	14.50	12.46
TFe_2O_3	6.87	7.06	7.48
MgO	2.66	3.46	3.68
CaO	5.59	3.55	4.79
Na_2O	5.06	4.32	4.47
K_2O	3.16	3.10	3.05
MnO	2.18	3.14	3.45
TiO_2	0.58	0.54	0.50
P_2O_5	3.45	2.15	3.08
C_{total}	0.16	0.14	0.16
LOI	9.72	9.84	10.38
Total	99.19	99.21	99.43
ppm			
F	2920	2170	3410
Cl	>20000	>20000	>20000
Co	192	254	200
Ni	340	582	569
Cu	312	380	362
Zn	150	181	202
V	127	159	138
Ba	315	633	482
Sc	45.8	31.3	34.3
Ga	17.5	18.9	18.2
Pb	48.1	92.4	91.3
Sr	342	264	285
Cr	29.6	39.5	33.6
Zr	153	144	154
Y	618	245	258
La	315	142	153
Ce	183	174	209
Pr	85.5	37.7	40.5
Nd	396	171	184
Sm	88.7	38.8	40.9
Eu	19.0	8.46	8.85
Gd	96.0	41.3	43.7
Tb	15.1	6.46	6.84
Dy	89.7	39.1	40.6
Ho	20.7	8.91	9.28

Er	53.7	23.1	24.5
Tm	7.52	3.11	3.42
Yb	44.6	19.0	21.3
Lu	6.60	2.75	3.16
∑REE	1421	715	789
∑REY	2039	960	1047
LREE	1087	571	636
HREE	333	143	152

Table S2. Mineral proportions of starting materials

Sample No.	64-30	64-46	64-55
Fe-chlorite	5.10	6.87	7.34
Montmorillonite	28.41	0.83	7.34
Illite	20.01	16.99	28.40
Pyrophyllite	0.96	7.68	1.15
Andesine	39.35	25.15	19.50
Anorthite	0.00	30.10	30.30
Heulandite	0.57	2.27	1.96
Ca-gmelinite	0.01	0.20	0.37
Calcite	0.00	1.14	0.26
Halite	1.70	0.17	0.38
Quartz	1.23	7.39	5.65
Rutile	0.03	0.05	0.04
Apatite	2.62	1.17	4.45
Total	99.99	100.01	100.00

Table S3. Run conditions and phase proportions

Run	P (GPa)	T (°C)	Duration (h)	Grt	Ap	Cpx	Mica	Kfs	Qtz/Coe	Melt	ΣR^2
Sample 64-30											
LMD39-30	3.0	900	24	7.8	7.9	58.4	1.9	23.2	0.9	/	2.6
LMD752-30	4.0	1000	120	/	7.6	52.3	/	/	/	40.1	1.8
Anhydrous				/	*8.3*	*56.9*	/	/	/	*34.8*	*2.2*
LMD755-30	4.0	900	24	12.6	9.6	44.4	23.9	/	9.5	/	1.9
LMD757-30	4.0	800	24	9.8	10.4	44.9	26.3	/	8.6	/	1.6
Sample 64-46											
LMD39-46	3.0	900	24	7.8	3.5	62.0	2.7	23.4	0.7	/	8.9
LMD752-46	4.0	1000	120	22.4	2.3	32.7	/	/	2.1	40.5	6.5
Anhydrous				*23.7*	*2.4*	*34.6*	/	/	*1.2*	*38.1*	*2.9*
LMD755-46	4.0	900	24	22.4	4.7	40.8	20.3	/	11.8	/	3.0
LMD757-46	4.0	800	24	23.1	4.7	35.3	24.5	/	12.4	/	8.4
Sample 64-55											
LMD39-55	3.0	900	24	18.4	4.7	53.0	7.0	16.6	0.3	/	2.9
LMD752-55	4.0	1000	120	12.9	5.8	35.4	/	/	/	45.9	7.9
Anhydrous				*14.6*	*6.6*	*40.0*	/	/	/	*38.7*	*8.4*
LMD755-55	4.0	900	24	22.3	7.3	42.1	16.6	/	11.7	/	0.9
LMD757-55	4.0	800	24	13.6	7.1	47.2	27.3	/	4.8	/	1.8

Note: Grt, garnet; Ap, apatite; Cpx, clinopyroxene; Kfs, K-feldspar; Qtz/Coe, quartz/coesite. ΣR^2: the summation of squared residuals obtained using phase compositions, mineral proportions, and bulk starting compositions. Mass balance of experiments in which melts occur, were firstly performed using initial compositions, and later the anhydrous (value in italic).

/ = not exist